Medium-range order in amorphous selenium: Molecular dynamics simulations

Kazuma Nakamura and Atsushi Ikawa
Department of Chemistry, Graduate School of Science, Kyoto University, Kitashirakawa, Sakyo-ku, Kyoto, 606-8502, Japan
(Received 23 September 2002; revised manuscript received 16 December 2002; published 14 March 2003)

In this paper we present a theoretical study on a glassy structure and infrared (IR)/Raman spectra of amorphous selenium (*a*-Se). The vibrational spectra are calculated for two-hundred independent amorphous samples obtained by performing molecular-dynamics (MD) simulations for one linear chain of 216 Se atoms. The interaction potential used in the MD simulation is constructed on the basis of *ab initio* molecular-orbital calculations (with the Hartree-Fock and second-order Møller-Plesset methods) for various Se clusters. The parameters in the bond-current and bond-polarizability models needed for the spectral calculations are also determined by the same *ab initio* approach. The calculated static structure factor, vibrational density of states, and IR/Raman spectra well reproduce experimental results. It is found that there exists a remarkable medium-range order in the disordered Se chain; i.e., a chain segment having four consecutive dihedral angles with alternate signs [i.e., $(+,-,+,-)$ or $(-,+,-,+)$] tends to be excluded from the chain structure, which is attributed to the steric hindrance effect existing in those configurations. By comparing the polarized Raman spectra for two different random chains with and without the above steric hindrance effect, we find that only the former spectrum exhibits a distinct peak at 80 cm^{-1} which is observed also in the experiment. Therefore the appearance of this peak provides useful information on the medium-range order existing in the disordered Se chain.

DOI: 10.1103/PhysRevB.67.104203 PACS number(s): 61.43.Fs, 78.30.−j, 63.50.+x

I. INTRODUCTION

Amorphous selenium (*a*-Se) has been widely investigated as a representative disordered system both experimentally and theoretically. In particular, optical properties associated with photoinduced structural changes such as the photoconductivity and photodarkening phenomena[1,2,27] have received much attention in semiconductor technologies. It is well known that the system undergoes the so-called semiconductor-metal transition[3,4] near the critical point ($T_c = 1860$ K, $p_c = 380$ bars,) which is also closely related to the structural changes in the liquid phase occurring at high temperatures. To deeply understand such various phenomena, it is highly desirable to obtain microscopic information on the disordered system.

The structure of *a*-Se has been currently considered as follows: (i) the major component is two-coordinated chain polymers with 10^3-10^4 Se atoms, while the fraction of ring molecules such as Se_7 and Se_8 is considerably small, (ii) bond lengths and bond angles in the disordered Se chain are approximately 2.35 Å and 105°, respectively, and (iii) dihedral angles tend to distribute around ±90° because of a lone-pair repulsion between the neighboring atoms. Such structural information on the short-range order has been confirmed through the viscosity experiment for liquid Se near the melting point,[5] NMR,[6] x-ray[7] and neutron-diffraction[8–10] measurements, extended x-ray-absorption fine structure,[11] infrared (IR)/Raman spectroscopy,[12–19] and also by performing recently developed tight-binding[20–22] and *ab initio*[23–27] molecular dynamics (MD) simulations.

There are many properties, however, which cannot be understood within the knowledge on the short-range order mentioned above. IR and Raman spectra are typical examples of such properties, since the induced dipole and polarizability responsible for these spectra extend spatially beyond the length scale associated with the short-range order.[28–30] In the case of *a*-Se, the IR and Raman peaks in the low-frequency bands (0–150 cm^{-1}) have not yet been assigned, and these assignments seem to require a theoretical analysis that takes into account a *medium-range* structure of the system. Although there are many MD simulations performed for *a*-Se,[20–27,31–36] these studies put emphasis on reproducing the short-ranged properties such as the static structure factor, and hence they are not helpful in assigning the low-frequency band.

Our aim in this paper is thus to perform a theoretical analysis on the IR and Raman spectra of *a*-Se, focusing especially on a possible medium-range order of the system. To this end we first construct an analytical valence force field model describing the intra- and interchain interactions based on *ab initio* molecular-orbital (MO) calculations. With this force field a set of MD simulations are performed to generate glassy samples of the disordered Se chain, which are subsequently used for calculating the IR and Raman spectra within the framework of the bond-current and bond-polarizability models. These analyses will show that there exists a medium-range order associated with *four consecutive dihedral angles* along the Se chain, which is related to the steric hindrance effect in the chain. We will also demonstrate that it does affect the polarized Raman spectra in the low-frequency band.

This paper is organized as follows: In Sec. II, we describe the interaction potential based on the *ab initio* MO calculations for various Se clusters. Details of the MD simulation, procedures for obtaining the vitreous structures, and comparisons between the calculated and experimental structure factors are given in Sec. III. We show in Sec. IV the theoretical vibrational density of states and IR/Raman spectra, together with a parametrization of the bond-current/bond-

polarizability models, and then compare them with the experimental results. Section V is devoted to assignments of the vibrational spectra and the analysis of a possible medium-range order in the disordered Se system. Concluding remarks are given in Sec. VI.

II. INTERACTION POTENTIAL

The total potential U_{total} for *one* covalent-bonded chain polymer is approximately divided into two parts,[29–33] i.e., the intrachain valence force field (VFF) U_{intra} and the nonbonded atoms interaction U_{NB},

$$U_{\text{total}} = U_{\text{intra}} + U_{\text{NB}}. \tag{1}$$

Here U_{intra} describes the potential associated with the chain backbone, while U_{NB} describes the excluded volume effect between nonbonded atoms.

To determine a set of parameters in the potential (see below), *ab initio* MO calculations were performed for various Se clusters using the restricted Hartree-Fock (RHF) and second-order Møller-Plesset perturbation (MP2) theories. We utilized the GAUSSIAN 98 suite[37] for this purpose, and employed a double-ζ, valence basis set optimizing for use of the effective core potential,[38] together with two sets of *d*-type polarization functions[39] ($\zeta_{d1}=0.489$, $\zeta_{d2}=0.144$) [ECP-41G(2*d*)]. We note here that the reliability of this basis set has been demonstrated in a previous work for a regular helical Se chain.[40]

A. Intrachain valence force field

In this work we employed a rather simple form of the intrachain valence force field, U_{intra}, which includes several terms such as stretching U_r, bending U_θ, and torsional U_ϕ potentials as well as coupling $U_{rr'}$ and $U_{r\theta}$ terms among them:

$$U_{\text{intra}} = U_r + U_\theta + U_\phi + U_{rr'} + U_{r\theta} \tag{2}$$

$$\begin{aligned} &= \frac{k_r}{2}\sum_n (r_n - \overline{r})^2 + \frac{k_\theta}{2}\sum_n (\theta_n - \overline{\theta})^2 \\ &+ \frac{V_\phi}{2}\sum_n \{1 - \cos 2(\phi_n - \overline{\phi})\} \\ &+ k_{rr'}\sum_n (r_{n-1} - \overline{r})(r_n - \overline{r}) \\ &+ k_{r\theta}\sum_n \{(r_{n-1} - \overline{r}) + (r_n - \overline{r})\}(\theta_n - \overline{\theta}). \end{aligned} \tag{3}$$

Here r_n, θ_n, and ϕ_n are the nth triplet of the internal variables (bond length, bond angle, and dihedral angle, respectively) of the chain, which are illustrated in Fig. 1(a), and $\overline{r}$, $\overline{\theta}$, and $\overline{\phi}$ represent their values at the equilibrium geometry. k_r, k_θ, $k_{rr'}$, and $k_{r\theta}$ stand for the harmonic force constants, and V_ϕ describes a rotational barrier of the dihedral angle. We emphasize that the above VFF is a ''minimal'' model for reproducing the experimental disordered structure and vibrational spectra. We first employed a slightly more complex functional form involving the couplings between the dihedral angle and other variables, but it was found that these couplings are not essential in reproducing the experimental results such as vibrational spectra. On the other hand, the two coupling terms in Eq. (2) (i.e., the stretch-stretch coupling $U_{rr'}$ and the stretch-bend coupling $U_{r\theta}$) were found to be crucially important in reproducing the experimental IR and Raman frequencies of the stretching band of *a*-Se (see Sec. V A). The details of the results were reported in Ref. 30.

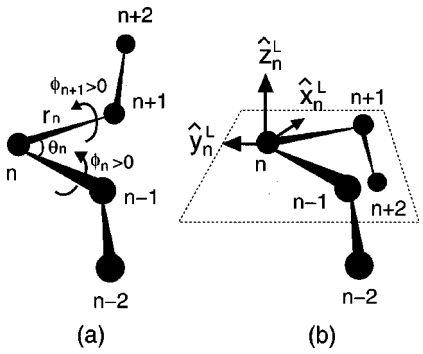

FIG. 1. Helixlike segment (a) and ringlike segment (b) in *a*-Se. The nth triplet of the internal variables (i.e., the bond length r_n, bond angle θ_n, and dihedral angle ϕ_n) is given in panel (a), while the definition of the nth local coordinate system $\{\hat{x}_n^L, \hat{y}_n^L, \hat{z}_n^L\}$ is given in panel (b). The central atom n in each segment is defined as the helixlike or ringlike atom (see Sec. V B).

To determine the VFF parameters above, we focus on two characteristic segments representing the basic building blocks of the disordered Se chain,[14] namely the *helixlike* segment and the *ringlike* segment depicted in Fig. 1. These segments are defined in terms of the signs of two consecutive dihedral angles ϕ_n and ϕ_{n+1} as

$$(\phi_n, \phi_{n+1}) = \begin{cases} (+,\ +) \text{ or } (-,\ -) & \text{for helixlike segment,} \\ (+,\ -) \text{ or } (-,\ +) & \text{for ringlike segment.} \end{cases} \tag{4}$$

With this definition, the segment depicted in Fig. 1(a) is helixlike since both the ϕ_n and ϕ_{n+1} angles are positive, while that in Fig. 1(b) is ringlike because $\phi_n>0$ and $\phi_{n+1}<0$. (We note here that the present classification is associated with five consecutive atoms in the disordered chain, and that the magnitude of the dihedral angles are not taken into account in the definition above.) Next we consider two types of finite Se chain molecules terminated by the hydrogen (H) atoms, $HSe_{11}H$, which contains a helixlike or ringlike segment at the center of the molecule. Then *ab initio* MO calculations were performed with the RHF plus MP2 methods to obtain their optimized geometries and associated force constants. The resulting VFF parameters are listed in Table I. We should note here that the equilibrium dihedral angle $\overline{\phi}$ and the rotational barrier V_ϕ were determined in a different manner; they were estimated by calculating a one-dimensional adiabatic potential energy curve (at the RHF level) as a function of the dihedral angle with all the other internal coordinates optimized geometrically.

The parameters used in the following MD simulations are defined basically as the average of the values for the helix-

TABLE I. Parameters in the intrachain valence force field U_{intra} [Eq. (2)] derived from *ab initio* MO calculations for two types of the chain molecule $HSe_{11}H$, which contains a helixlike or ringlike segment at each molecular center. The $\overline{r}$, $\overline{\theta}$, k_r, k_θ, $k_{rr'}$, and $k_{r\theta}$ values were evaluated at the MP2 level, while the $\overline{\phi}$ and V_ϕ values were estimated at the RHF level. The parameters used in the MD simulation (fourth column) are the averages of the values for the helixlike and ringlike configurations except for $\overline{\theta}$, $\overline{\phi}$, and k_r.

	Helixlike	Ringlike	Simulation
$\overline{r}$ (Å)	2.3537	2.3530	average
$\overline{\theta}$ (°)	103.34	104.93	106.0
$\overline{\phi}$ (°)	80.46	90.93	90.0
k_r (hartree/bohr^2)	0.1085	0.1089	average$\times$0.9
k_θ (hartree/rad.^{2})	0.1652	0.1772	average
V_ϕ (hartree)	0.0065	0.0058	average
$k_{rr'}$ (hartree/bohr^2)	0.0153	0.0160	average
$k_{r\theta}$ (hartree/bohr/rad.)	0.0161	0.0172	average

like and ringlike configurations. Since we are interested in constructing the potential function that can reproduce the experimental IR/Raman spectra, we made the following adjustments on the parameters (see the fourth column in Table I): first, the stretching force constant k_r was scaled by a factor of 0.9 so as to reproduce the experimental frequencies, which is related to a redshift of the frequencies in condensed phase due to a through-space charge-transfer effect.[19,41] Second, we set the equilibrium bond angle $\overline{\theta}$ to 106°, which is important in reproducing the experimental relative position of the stretching IR and Raman peaks (see Sec. V A). Also the equilibrium dihedral angle $\overline{\phi}$ was set to 90° so that the torsional potential, $(V_\phi/2)\{1-\cos 2(\phi-\overline{\phi})\}$, should satisfy an inversion symmetry about $\phi=0°$.

B. Nonbonded atoms interaction

The nonbonded atoms interaction in Eq. (1), U_{NB}, is described as the sum of pairwise potentials $U(R)$,

$$U_{\text{NB}}=\sum_{n\geqslant m+3} U(R_{nm}) \tag{5}$$

$$=\sum_{n\geqslant m+3}\left\{A\left(\frac{1}{R_{nm}}\right)^{\eta_A}-B\left(\frac{1}{R_{nm}}\right)^{\eta_B}\right\}, \tag{6}$$

where R_{nm} is the distance between nonbonded atoms n and m in the chain.

To determine the repulsion parameters (A,η_A) in the potential, we first calculated the interaction energies between various monomers (HSe_3H and HSe_4H) with the RHF method, changing the distance between the monomers. These configurations were chosen by considering the orientation of lone-pair orbitals or covalent bonds in the dimer, and a total of 184 configurations were sampled to examine the repulsive interactions. The A and η_A parameters were then determined by fitting them to the resulting *ab initio* energies, which are shown in Table II. The least-squares fitting error is about 2 kcal/mol, which suggests a reasonable agreement between the fitted potential and the *ab initio* one, particularly considering the simple isotropic form of the potential function.

TABLE II. Determined parameters in the pairwise potential $U(R)$ [Eq. (6)].

A (hartree·bohr^8)	18 045.74
η_A	8
B (hartree·bohr^6)	416.0
η_B	6

The attraction parameters (B,η_B) in the potential were determined so that the simulated density should agree with the experimental density[42] ($\rho_{\text{expt.}}=4.280$ g/cm^3); i.e., these parameters were empirically determined after a number of MD simulations with different sets of (B,η_B) values. We plot in Fig. 2 the total potential energy per particle (U_{total}/N) as a function of the density ρ. The potential energy at each density was evaluated for the optimized geometry of the amorphous sample obtained from the MD simulation with $B=416.0$ and $\eta_B=6$ (in Table II). A parabolic fit was then carried out for the resulting potential curve. The density thus obtained becomes 4.284 g/cm^3.

III. MOLECULAR DYNAMICS SIMULATION AND PREPARATION OF VITREOUS STRUCTURE

The MD simulations were performed for a system containing *one* linear chain of 216 atoms with a periodic boundary condition. The length of the periodic cell was chosen at 18.774 Å, which gives the density of 4.280 g/cm^3 corresponding to the experimental value.[42] The equation of motion was integrated using the velocity-Verlet argolithm[43] with a time step Δt of 2×10^{-15} sec.

Amorphous structures were obtained through the following four steps (also shown schematically in Fig. 3): (i) A random chain was generated as an initial configuration with the bond lengths r_n and bond angles θ_n fixed at their equilibrium values, and with the dihedral angles ϕ_n randomly distributed over the interval $-180°<\phi_n<180°$. This chain was equilibrated with an MD simulation of 1 ns at a rela-

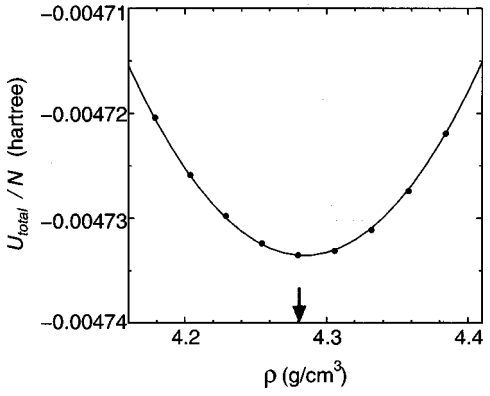

FIG. 2. Total potential energy per particle U_{total}/N as a function of the density ρ. An arrow indicates the position of the experimental density ($\rho_{\text{expt.}}=4.280$ g/cm^{-3}) (Ref. 42).

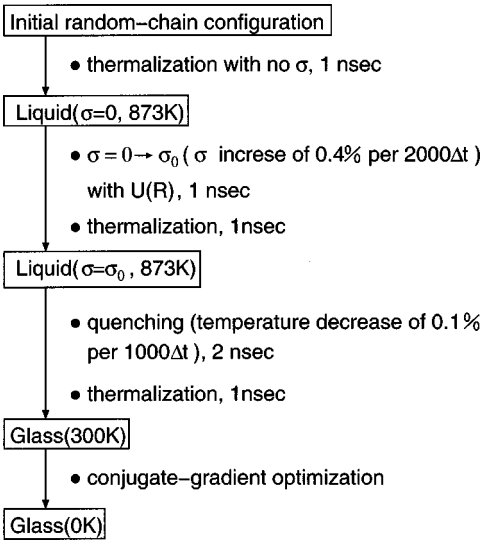

FIG. 3. Schematic diagram of the computational procedure for obtaining glassy structures of *a*-Se.

tively high temperature of 873 K. We note here that the excluded volume effect was completely neglected at this stage; i.e., only the intrachain valence force field U_{intra} of Eq. (2) was included in the simulation above. (ii) To recover the excluded volume effect, we introduced the nonbonded atoms interaction U_{NB} gradually into the system. For this purpose it is convenient to rewrite the pairwise potential in Eq. (6) in terms of the equilibrium distance $\sigma_0(=4.02\ \text{Å})$ corresponding to the potential minimum as

$$U(R)=a\left(\frac{\sigma_0}{R}\right)^{\eta_A}-b\left(\frac{\sigma_0}{R}\right)^{\eta_B}, \tag{7}$$

where the a and b values are defined by the equations of $a\sigma_0^{\eta_A}=A$ and $b\sigma_0^{\eta_B}=B$, respectively. The σ_0 parameter in the potential was first artificially set to zero, and then we made it recover the original value (4.02 Å) at the rate of 0.4% per 2000 time steps. After the recovery process we carried out an equilibration run of 1 ns at the liquid temperature. (iii) The resulting structure was then thermally quenched from the liquid state at 873 K to the glassy state at 300 K via a stepwise rescaling of the atomic velocity. The rate of temperature decrease is 0.1% per 1000 time steps corresponding to 0.287×10^{12} K/sec. After the quenching process, the system was again thermalized at the temperature for 1 ns. (iv) Finally we performed a geometry optimization of the chain using the conjugate-gradient method;[44] i.e., the system was quenched to the zero-temperature limit, thus resulting in an amorphous structure of interest. By repeating the four procedures above we generated a set of 200 independent vitreous structures, which were subsequently used to evaluate the ensemble average of static and dynamic properties.

To check the reliability of the vitreous structures thus obtained, we calculated the static structure factor defined by

$$S(q)=\frac{1}{N}\left\langle \sum_n \sum_m e^{i\mathbf{q}\cdot(\mathbf{R}_m-\mathbf{R}_n)}\right\rangle, \tag{8}$$

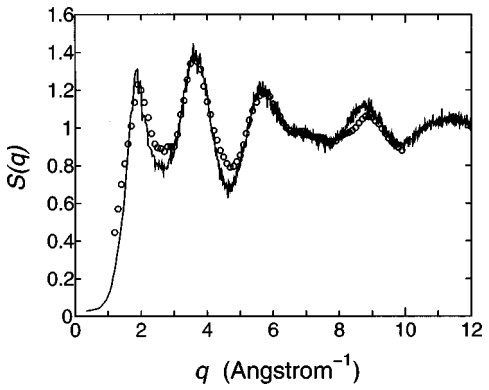

FIG. 4. Comparison between the calculated (solid line) and experimental (Ref. 10) (open circle) static structure factors of *a*-Se at 300 K.

where $\mathbf{q}$ denotes a scattered wave vector, $\mathbf{R}_n$ is the position of the nth atom, and $\langle\cdots\rangle$ represents the ensemble average. Figure 4 shows the comparison of the calculated $S(q)$ at 300 K (solid line) with the result of the recent neutron-scattering measurement[10] (open circle). As seen in the figure, the calculated result agrees quite well with the experimental one, including peak positions at 1.9, 3.7, 5.3, and 8.9 Å^{-1} as well as the shoulderlike feature around 7.0 Å^{-1}.

Although this good agreement is very encouraging, we need to emphasize that the static structure factor $S(q)$ is a quantity rather insensitive to the details of the potential function; various other chain models can also reproduce the experimental structure factor rather well. For instance, the experimental $S(q)$ can be reproduced by the so-called nearly free rotating chain model[8,9] having the rigid bond lengths and angles but the randomly distributed dihedral angles. On the other hand, the dihedral angles in our samples are distributed around $\pm90°$ with the full width at half maximum of 40°. Thus it is clear that $S(q)$ is almost dominated by a *short-range order* (i.e., two-body and three-body correlations) but is very insensitive to a *medium-range order* related to more than four-body correlations.

IV. VIBRATIONAL SPECTRA

As mentioned above, the static structure factor $S(q)$ is a quantity rather insensitive to a medium-range order in the system. Hence it is necessary to go beyond that quantity in order to investigate the latter, and to this end we consider the vibrational properties of *a*-Se such as the IR and Raman spectra in the following sections.

A. Vibrational normal modes and density of states

Vibrational normal modes needed for the calculation of the vibrational spectra are obtained by diagonalizing a (mass-scaled) force constant matrix for the geometry-optimized vitreous structure. The matrix elements are defined as

$$D_{n\alpha,m\beta}=\left(\frac{1}{M}\right)\frac{\partial^2 U_{\text{total}}}{\partial u_\alpha(n)\partial u_\beta(m)}, \tag{9}$$

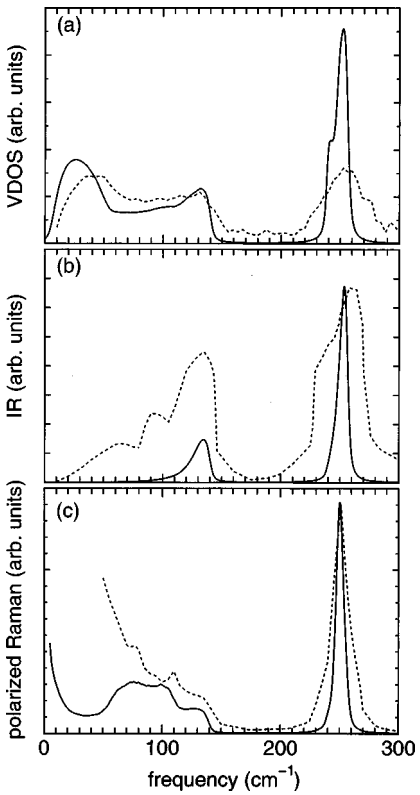

FIG. 5. Comparison of vibrational spectra between theory (solid line) and experiment (dotted line): (a) vibrational density of states (VDOS); (b) IR spectrum; (c) polarized Raman spectrum at 300 K. The experimental VDOS and Raman spectrum are taken from Refs. 45 and 14, respectively. The experimental IR spectrum is taken from Ref. 12 for the frequency range of 10–80 cm^{-1} and from Ref. 14 for 80–300 cm^{-1}. A Lorentzian broadening of 1.5 cm^{-1} is applied to the calculated spectra.

where U_{total} is the total potential energy in Eq. (1), $u_\alpha(n)$ stands for the Cartesian displacement of the nth atom along the coordinate axis α, and M is the atomic mass of Se. The eigenvectors $\{Q_i\}$ and eigenvalues $\{\omega_i^2\}$ thus obtained describe the vibrational normal modes and the associated frequencies. In actual calculations the above force-constant matrix was evaluated via finite difference of the analytical forces with respect to the atomic displacements.

The vibrational density of states (VDOS) can be written using the eigenfrequencies $\{\omega_i\}$ as

$$\rho(\omega)=\left\langle \sum_i \delta(\omega-\omega_i)\right\rangle, \tag{10}$$

where the angular bracket indicates an ensemble average over the 200 structural samples generated in the preceding section. We compare in Fig. 5(a) the calculated VDOS (solid line) with the experimental one (dotted line) obtained from the inelastic neutron-scattering measurement.[45] The VDOS consists of the stretching ($230 \leqslant \omega \leqslant 270$ cm^{-1}), bending ($50 \leqslant \omega \leqslant 150$ cm^{-1}), and torsional/intermolecular ($0 \leqslant \omega \leqslant 50$ cm^{-1}) bands. It is seen from this figure that the calculated VDOS is qualitatively in good agreement with the experimental result over the whole frequency range.

B. IR spectrum

The IR spectrum is written in terms of the derivative of a total dipole moment $\boldsymbol{\mu}$ with respect to the normal mode Q_i,

$$I(\omega)=\left\langle \sum_i \left|\frac{\partial \boldsymbol{\mu}}{\partial Q_i}\right|^2 \delta(\omega-\omega_i)\right\rangle, \tag{11}$$

where (and from now on) we omit a proportionality constant independent of ω. For numerical calculations it is more convenient to express the derivative $\partial\boldsymbol{\mu}/\partial Q_i$ in terms of derivatives with respect to the Cartesian coordinates as

$$\frac{\partial \boldsymbol{\mu}}{\partial Q_i}=\sum_n \sum_\alpha \frac{\partial \boldsymbol{\mu}}{\partial u_\alpha(n)} \frac{\partial u_\alpha(n)}{\partial Q_i}. \tag{12}$$

Here the first factor $\partial\boldsymbol{\mu}/\partial u_\alpha(n)$ on the right-hand side is called a dynamical-charge tensor and describes the response of the total dipole to the displacement of each atom.

For a polymeric chain the system dipole may be divided into through-bond-type and through-space-type contributions. The former dipole results from the electron transfer through covalent bonds in the chain, while the latter originates from the electron transfer between nonbonded atoms due to the spatial overlap of the (localized) molecular orbitals. In the present work we neglect the latter contribution for the sake of simplicity. We also make a further approximation to the through-bond charge transfer; i.e., the system dipole will be described using the following bond-current (BC) model,[15,40,46–48]

$$\boldsymbol{\mu}=\sum_n \left(\frac{J_r}{r}(\Delta r_{n-1}-\Delta r_n)(\mathbf{r}_{n-1}+\mathbf{r}_n)+J_\theta \Delta\theta_n(\mathbf{r}_{n-1}-\mathbf{r}_n)\right), \tag{13}$$

where $\mathbf{r}_n$ denotes the bond vector $\mathbf{R}_{n+1}-\mathbf{R}_n$, and Δr_n and $\Delta\theta_n$ represent $r_n-\overline{r}$ and $\theta_n-\overline{\theta}$, respectively. Within the above model the dipole moment is determined by only the two parameters J_r and J_θ, which describe through-bond electronic currents induced by local stretching and bending motions, respectively.[15,40,47]

Numerical values of these BC parameters (J_r, J_θ) were determined by fitting the approximate dynamical-charge tensors derived with the BC model to those obtained from *ab initio* electronic structure calculations. The latter *ab initio* calculations at the MP2 level were performed for the central atoms in the $HSe_{11}H$ molecules having a helixlike or ringlike configuration (Fig. 1). The dipole derivative was estimated by the numerical differentiation of the analytic dipole with respect to the atomic displacement. We also introduced an additional p-type diffuse function[49] ($\zeta_p=0.0328$) [ECP-41G+(2d)] into the basis set in order to accurately describe polarization properties.[50] We show in Table III the dynamical-charge tensors thus obtained from the *ab initio* calculations and from the BC model. These tensors are expressed in terms of the local coordinate system $\{\hat{x}_n^L,\hat{y}_n^L,\hat{z}_n^L\}$ [see Fig. 1(b)], where the y axis is taken to be the opposite direction of the bisector of the $(n-1)$-n-$(n+1)$ angle, the x axis is perpendicular to this bisector and in the $(n-1)$-n-$(n+1)$ plane, and the z axis is orthogonal to both the

TABLE III. Dynamical-charge and polarizability-derivative tensors for the helixlike and ringlike configurations obtained from the *ab initio* MO method [MP2/ECP-41G+(2*d*)] and from the bond-current (BC)/bond-polarizability (BP) models. The tensors are represented in the local coordinates [Fig. 1(b)]. Unit: atomic unit.

$\partial\mu_i/\partial\xi_j$			$\partial\chi_{ij}/\partial\xi_x$			$\partial\chi_{ij}/\partial\xi_y$			$\partial\chi_{ij}/\partial\xi_z$		
(helixlike configuration, *ab initio*)											
0.085	0	0.046	0	5.57	0	2.91	0	−0.21	0	1.26	0
0	−0.049	0	5.57	0	−0.79	0	13.53	0	1.26	0	4.88
−0.108	0	−0.045	0	−0.79	0	−0.21	0	4.36	0	4.88	0
(helixlike configuration, BC/BP model)											
0.107	0	0.054	0	5.29	0	2.84	0	0	0	2.46	0
0	−0.043	0	5.29	0	−0.33	0	11.96	0	2.46	0	5.72
−0.128	0	−0.065	0	−0.33	0	0	0	6.47	0	5.72	0
(ringlike configuration, *ab initio*)											
0.119	0	0	0	5.29	−0.18	0.62	0	0	4.84	0	0
0	−0.026	0.044	5.29	0	0	0	11.22	5.42	0	0.93	4.18
0	−0.146	−0.085	−0.18	0	0	0	5.42	7.21	0	4.18	10.44
(ringlike configuration, BC/BP model)											
0.102	0	0	0	5.48	−0.04	1.91	0	0	5.24	0	0
0	−0.027	0.026	5.48	0	0	0	11.08	0.13	0	4.15	5.15
0	−0.121	−0.070	−0.04	0	0	0	0.13	5.57	0	5.15	6.76

x and *y* axes making a right-handed coordinate system. As found from the table the fitting accuracy is quite good for both the configurations with the least-squares error of 0.012 (a.u.). The resulting parameters (J_r, J_θ) are given in Table IV.

We show in Fig. 5(b) the IR spectrum calculated via Eq. (11) (solid line), together with the experimental result[12,14] (dotted line). Our result reproduces the experimental main bending and stretching peaks at 135 and 255 cm^{-1}, respectively, whereas the intensity of the bending peak is somewhat underestimated in the theoretical result. Unfortunately, the calculated spectrum does not reproduce either the experimental bending subpeaks at 60 and 95 cm^{-1} or the stretching shoulder peak at 238 cm^{-1}. These deficiencies may be attributed to the neglect of through-space charge transfers between nonbonded atoms in the theoretical treatment above.[29]

C. Polarized Raman spectrum

Next we consider the polarized Raman spectrum at a finite temperature, which can be written as

$$S(\omega)=\frac{\hbar}{\omega(1-e^{-\beta\hbar\omega})}\left\langle\sum_i\left[\frac{1}{3}\mathrm{Tr}\left(\frac{\partial\boldsymbol{\chi}}{\partial Q_i}\right)\right]^2\delta(\omega-\omega_i)\right\rangle, \tag{14}$$

where $\boldsymbol{\chi}$ is a total polarizability tensor of the system, and $\beta=1/k_BT$. Similarly to the case of the dipole derivative, the polarizability derivative is also rewritten in terms of those with respect to the Cartesian displacements as

$$\frac{\partial\boldsymbol{\chi}}{\partial Q_i}=\sum_n\sum_\alpha\frac{\partial\boldsymbol{\chi}}{\partial u_\alpha(n)}\frac{\partial u_\alpha(n)}{\partial Q_i}. \tag{15}$$

The derivative $\partial\boldsymbol{\chi}/\partial u_\alpha(n)$ is referred to as a polarizability-derivative tensor and expresses the response of the total polarizability to atomic displacements.

In parallel to the treatment of the dipole moment in the previous subsection, we treat the system polarizability using the so-called bond-polarizability (BP) model,[48,51] in which the total polarizability is approximated by a sum of polarizability tensors for the individual bonds with a cylindrical symmetry. With this model the total polarizability of a simple chain system can be written as

$$\boldsymbol{\chi}=\sum_n\left[\alpha_n\mathbf{I}+\beta_n\left(\hat{r}_n\hat{r}_n^t-\frac{1}{3}\mathbf{I}\right)\right], \tag{16}$$

where $\mathbf{I}$ is a 3×3 identity matrix, $\hat{r}_n=\mathbf{r}_n/r_n$, and α_n and β_n describe isotropic and anisotropic parts of the bond polarizability, respectively. We expand the α_n and β_n terms up to the first order in the internal variables as follows:

$$\alpha_n=\alpha_r\Delta r_n+\alpha_\theta(\Delta\theta_n+\Delta\theta_{n+1}), \tag{17}$$

TABLE IV. Determined parameters in the bond-current (BC) [Eq. (13)] and bond-polarizability (BP) [Eq. (16)] models. Unit: atomic unit.

BC model	J_r	0.0961
	J_θ	−0.0365
BP model	α_r	8.137
	α_θ	6.039
	β_r	8.761
	β_θ	11.733
	γ	3.222

$$\beta_n = \beta_r \Delta r_n + \beta_\theta (\Delta\theta_n + \Delta\theta_{n+1}) + \gamma \overline{r}. \quad (18)$$

Here the expansion coefficients (α_r, β_r) and $(\alpha_\theta, \beta_\theta)$ represent the changes in the polarizability of the nth bond by the local stretching and bending motions, respectively, while γ expresses the anisotropy of the static bond polarizability. It should be noted that the above functional form in Eqs. (17) and (18) differs from the conventional BP model in that the former includes the dependence of $\boldsymbol{\chi}$ on the bond angles (i.e., α_θ and β_θ) explicitly while the latter does not. We found that this extension is essential for reproducing the experimental bending Raman spectrum.

The BP parameters (α_r, α_θ, β_r, β_θ, γ) were determined with essentially the same fitting procedure as that of the BC parameters. *Ab initio* polarizability-derivative tensors were obtained by numerically differentiating the dynamical-charge tensor obtained above with respect to the applied electric field. We give in Table III the resulting *ab initio* polarizability-derivative tensors, together with the fitted model ones. Although some disagreements are seen in the case of the ringlike configuration, the accuracy of the parameter fitting is reasonably good as a whole with the least-squares fitting error of 1.35 (a.u.). The fitted BP parameters are listed in Table IV.

Figure 5(c) shows a comparison between the polarized Raman spectrum at 300 K obtained with Eq. (14) (solid line) and the experimental result[14] (dotted line). Our calculated spectrum reproduces the experimental sharp stretching peak at about 250 cm^{-1} and broad bending peaks around 80, 100, and 132 cm^{-1}. We should point out that our result also reproduces a slight redshift of the stretching Raman peak from the IR peak seen in the experimental spectra (theory, $\omega_{\mathrm{Raman}} = 250\ cm^{-1}$ and $\omega_{\mathrm{IR}} = 253\ cm^{-1}$; experiment, $\omega_{\mathrm{Raman}} = 250\ cm^{-1}$ and $\omega_{\mathrm{IR}} = 255\ cm^{-1}$), which will be examined further in the next section.

V. DISCUSSION

In this section we perform assignments for the calculated vibrational spectra of *a*-Se, particularly focusing on the following:

(i) The relative positions of the stretching IR (253 cm^{-1}) and Raman (250 cm^{-1}) peaks.
(ii) The physical origin of the three peaks (80, 100, and 132 cm^{-1}) appearing in the bending Raman spectrum.

We will examine the first issue through a comparison with vibrational spectra of a regular helix (Sec. V A), while we will analyze the second issue via use of an approximate formula for the bending Raman spectrum, and discuss a medium-range order of *a*-Se responsible for the spectrum in the frequency domain of interest (Sec. V B).

A. Comparison with the regular helix

The regular helix has a clear advantage that it is straightforward to assign the related spectrum: First, its vibrational property can be understood in terms of a dispersion relation connecting the frequency ω and the wave number $\tilde{q}$, which can be obtained using the Bloch theorem in a normal-mode analysis.[40] Second, its vibrational spectra can be assigned in terms of the rotational angle τ of the helix;[40,52] the IR active modes are the phonon modes with the wave number $\tilde{q}=0$ or τ, while the Raman active modes correspond to the $\tilde{q}=0$, τ, or 2τ phonon modes.[53] Since *a*-Se consists primarily of long chain polymers, we expect that the spectral features of the regular helix will also appear in the spectra of *a*-Se at least qualitatively.

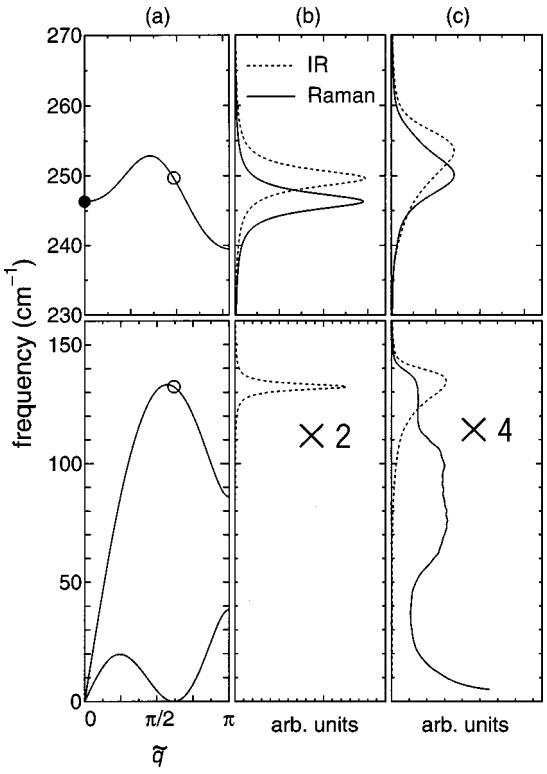

FIG. 6. Calculated phonon dispersion (a) and vibrational spectra of the regular helix (b) and *a*-Se (c). A Lorentzian broadening of 1.5 cm^{-1} is applied to the calculated spectra. Upper panels: frequency range for the stretching band (230–270 cm^{-1}). Lower panels: frequency range for the bending and torsional/intermolecular bands (0–160 cm^{-1}). Filled and open circles in the panel (a) refer to the $\tilde{q}=0$ and $\tilde{q}=\tau$ positions, respectively, where τ is the rotational angle of the regular helix.

We show in Fig. 6 the phonon dispersion curve (a) and the vibrational spectra (b) of the regular helix, and compare them with the spectra of *a*-Se (c). The calculations for the regular helix and *a*-Se were performed using the same force field and the BC/BP models. The IR spectrum of the regular helix exhibits a peak at the position of $\tilde{q}=\tau$ [open circle in the panel (a)], while the *polarized* Raman peak is at the position of $\tilde{q}=0$ (filled circle). (We note in passing that the $\tilde{q}=0$ mode is not IR active though it is allowed by the selection rule; this is simply because no dipole moment is induced by the mode.) As found from the figure the stretching phonon dispersion of the regular helix is a *convex* function of the wave number $\tilde{q}$; the frequency $\omega(\tilde{q})$ in this band increases from $\tilde{q}=0$ to $\tilde{q}=\pi/2$, and then decreases from $\tilde{q}=\pi/2$ to $\tilde{q}=\pi$.[54] Hence in the case of the regular helix, the stretching frequency of the IR absorption becomes higher than that of the Raman scattering. We should point out that a

similar tendency is also observed in the amorphous phase, indicating that the similar (virtual) phonon dispersion relation still remains in the vibrational characters of *a*-Se.[30] We can also see a similar correspondence in the bending IR spectrum; i.e., the bending IR peak of the regular helix (132 cm^{-1}) agrees with that of *a*-Se (135 cm^{-1}).

A significant difference appears in the case of the bending Raman spectra. That is, while the regular helix exhibits no intensity in this band, *a*-Se shows three bending peaks at 80, 100, and 132 cm^{-1}. This spectral difference seems to arise from their structural differences;[14] the former consists only of helixlike segments, whereas the latter includes ringlike segments in addition to the helixlike ones. Therefore, to understand the physical origin of the bending peaks above, it is necessary to examine the role of the ringlike segments existing in the disordered Se chain.

B. Effect of the medium-range order on the bending Raman spectrum

Here we derive an approximate formula for the bending Raman spectrum and demonstrate that structural correlations among consecutive ringlike segments strongly affect the low-frequency band of the Raman spectra. First, we define the reduced polarized Raman spectrum $S_R(\omega)$ by removing the pre-factor of the angular bracket in Eq. (14) as

$$S_R(\omega)=\frac{2\omega(1-e^{-\beta\hbar\omega})}{\hbar}S(\omega)=\left\langle \sum_i \left[\frac{\partial\overline{\chi}}{\partial Q_i}\right]^2 \delta(\omega-\omega_i)\right\rangle, \tag{19}$$

with $\partial\overline{\chi}/\partial Q_i=(1/3)\mathrm{Tr}(\partial\boldsymbol{\chi}/\partial Q_i)$, which is more suitable for discussing the dependence of the Raman spectra on the structure of *a*-Se. Next, we define a helixlike or ringlike *atom* as being the central atom of a helixlike or ringlike segment. According to this definition, the atom *n* in Fig. 1(a) are specified as a helixlike atom since the five atoms ($n-2$ to $n+2$) constitute a helixlike segment. Notice that any atom in the chain can be classified as helixlike or ringlike by considering the neighboring five atoms. Since a disordered chain is characterized by the sequence of helixlike and ringlike atoms, we divide the derivative $\partial\overline{\chi}/\partial Q_i$ into the following six terms:

$$\begin{aligned}\frac{\partial\overline{\chi}}{\partial Q_i}&=\sum_n\sum_\alpha \frac{\partial\overline{\chi}}{\partial\xi_\alpha(n)}\frac{\partial\xi_\alpha(n)}{\partial Q_i}\\ &=\sum_n^{\mathrm{HLA}}\left(\frac{\partial\overline{\chi}}{\partial\xi_x(n)}\frac{\partial\xi_x(n)}{\partial Q_i}+\frac{\partial\overline{\chi}}{\partial\xi_y(n)}\frac{\partial\xi_y(n)}{\partial Q_i}\right.\\ &\quad\left.+\frac{\partial\overline{\chi}}{\partial\xi_z(n)}\frac{\partial\xi_z(n)}{\partial Q_i}\right)+\sum_m^{\mathrm{RLA}}\left(\frac{\partial\overline{\chi}}{\partial\xi_x(m)}\frac{\partial\xi_x(m)}{\partial Q_i}\right.\\ &\quad\left.+\frac{\partial\overline{\chi}}{\partial\xi_y(m)}\frac{\partial\xi_y(m)}{\partial Q_i}+\frac{\partial\overline{\chi}}{\partial\xi_z(m)}\frac{\partial\xi_z(m)}{\partial Q_i}\right),\end{aligned} \tag{20}$$

where $\boldsymbol{\xi}(n)$ is the displacement vector of the *n*th atom in the local coordinates, and "HLA" and "RLA" in the summation denote the helixlike atom and the ringlike atom, respectively. Since the polarizability derivatives expressed in the local coordinates $\{\partial\overline{\chi}/\partial\boldsymbol{\xi}(n)\}$ are nearly *site independent*, we can approximate the derivatives as follows:

$$\left(\frac{\partial\overline{\chi}}{\partial\xi_x(n)},\frac{\partial\overline{\chi}}{\partial\xi_y(n)},\frac{\partial\overline{\chi}}{\partial\xi_z(n)}\right)\simeq(0,\alpha_r,0),\quad n\in\mathrm{HLA}, \tag{21}$$

$$\left(\frac{\partial\overline{\chi}}{\partial\xi_x(m)},\frac{\partial\overline{\chi}}{\partial\xi_y(m)},\frac{\partial\overline{\chi}}{\partial\xi_z(m)}\right)\simeq(0,\alpha_r,\alpha_\theta),\quad m\in\mathrm{RLA}. \tag{22}$$

Hence an isotropic induced-polarizability α_r term arises from the local *y* displacement of the helixlike atom, while two induced α_r and α_θ terms are for the local *y* and *z* displacements of the ringlike atom, respectively.[14] Substituting Eqs. (21) and (22) into Eq. (20) yields

$$\frac{\partial\overline{\chi}}{\partial Q_i}\simeq\delta\overline{\chi}^{\,i}_{\mathrm{HLA},y}+\delta\overline{\chi}^{\,i}_{\mathrm{RLA},y}+\delta\overline{\chi}^{\,i}_{\mathrm{RLA},z}, \tag{23}$$

with

$$\delta\overline{\chi}^{\,i}_{\mathrm{HLA},y}=\alpha_r\sum_n^{\mathrm{HLA}}\frac{\partial\xi_y(n)}{\partial Q_i}, \tag{24}$$

$$\delta\overline{\chi}^{\,i}_{\mathrm{RLA},y}=\alpha_r\sum_m^{\mathrm{RLA}}\frac{\partial\xi_y(m)}{\partial Q_i}, \tag{25}$$

$$\partial\overline{\chi}^{\,i}_{\mathrm{RLA},z}=\alpha_\theta\sum_m^{\mathrm{RLA}}\frac{\partial\xi_z(m)}{\partial Q_i}, \tag{26}$$

which suggests that the Raman-scattering intensity for the normal mode Q_i becomes

$$\left(\frac{\partial\overline{\chi}}{\partial Q_i}\right)^2=(\delta\overline{\chi}^{\,i}_{\mathrm{HLA},y})^2+(\delta\overline{\chi}^{\,i}_{\mathrm{RLA},y})^2+(\delta\overline{\chi}^{\,i}_{\mathrm{RLA},z})^2+\text{cross terms}. \tag{27}$$

By substituting Eq. (27) into Eq. (19), we can decompose the reduced polarized Raman spectrum in the bending band into the individual contributions. Figure 7(a) displays the decomposed Raman spectrum thus obtained, which clearly shows that the three peaks in the full spectrum (thick solid line) are dominated only by the contribution of the $(\delta\overline{\chi}^{\,i}_{\mathrm{RLA},z})^2$ term in Eq. (27) (thin solid line).

This fact implies a further approximation to the polarizability derivative in Eq. (23), that is, we may keep only the third term in Eq. (23) as

$$\frac{\partial\overline{\chi}}{\partial Q_i}\simeq\alpha_\theta\sum_m^{\mathrm{RLA}}\frac{\partial\xi_z(m)}{\partial Q_i}. \tag{28}$$

With this approximation, the Raman intensity can be rewritten in terms of structural correlation functions. This is accomplished by first introducing a characteristic function $\{f_m\}$ that selects only the ringlike atoms,

$$f_m=\begin{cases}1, & m\in\mathrm{RLA},\\ 0, & m\in\mathrm{HLA},\end{cases} \tag{29}$$

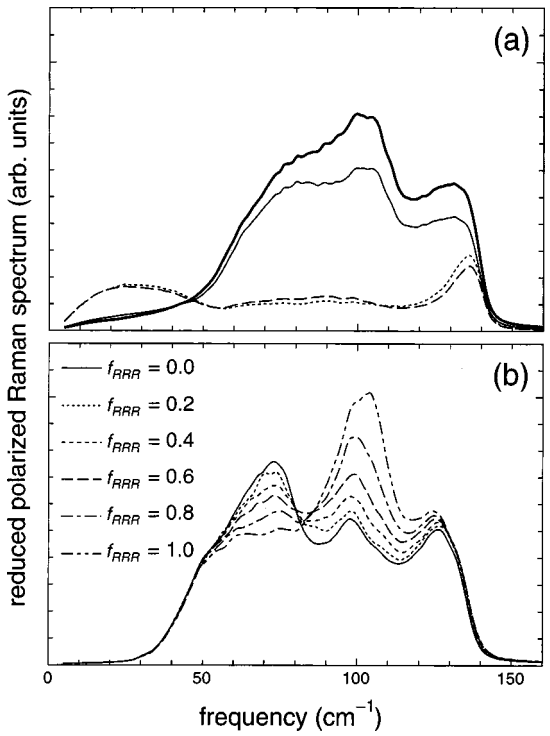

FIG. 7. (a) Decomposition of the reduced polarized bending Raman spectrum (thick solid line) for the generated MD samples into the $(\delta\overline{\chi}^{\rightarrow}_{\mathrm{HLA},y})^2$ (dotted line), $(\delta\overline{\chi}^{\rightarrow}_{\mathrm{RLA},y})^2$ (dashed line), and $(\delta\overline{\chi}^{\rightarrow}_{\mathrm{RLA},z})^2$ (thin solid line) terms [Eq. (27)]. (b) Dependence of the reduced polarized bending Raman spectrum of the artificial Se chain on the steric-hindrance parameter f_{RRR} $(0 \leqslant f_{\mathrm{RRR}} \leqslant 1)$. The results were obtained by taking an ensemble average over one-thousand configurations.

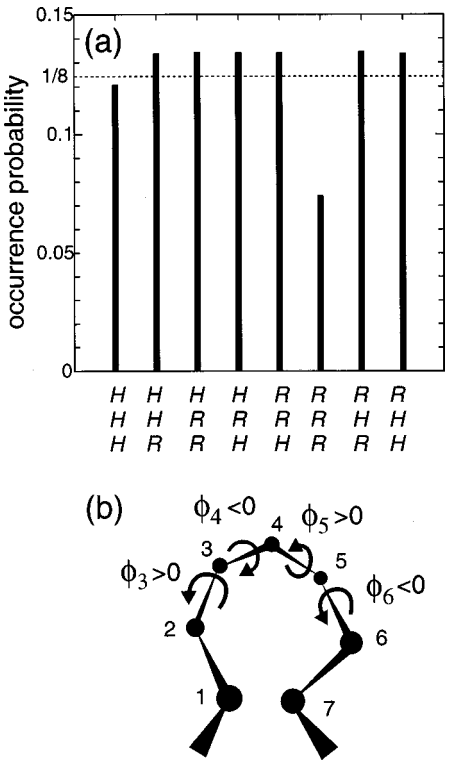

FIG. 8. (a) Pattern statistics for seven consecutive atoms in the disordered Se chain. The symbols "*H*" and "*R*" denote the classification of three consecutive segments included in the seven-atom configuration (i.e., the sequence of helixlike or ringlike segments). A dotted line represents the average value $(\frac{1}{8})$ of the occurrence probabilities for the listed eight configurations. (b) The RRR configuration, in which four consecutive dihedral angles $(\phi_3, \phi_4, \phi_5, \phi_6)$ take a sign pattern of $(+, -, +, -)$. The first and seventh atoms in the configuration tend to overlap with each other, and hence the configuration tends to be excluded from the chain structure due to a large steric repulsion energy.

to remove the limitation on the summation

$$\frac{\partial\overline{\chi}}{\partial Q_i} = \alpha_\theta \sum_m f_m \frac{\partial \xi_z(m)}{\partial Q_i}, \tag{30}$$

and taking the square of the above equation to give

$$\left[\frac{\partial\overline{\chi}}{\partial Q_i}\right]^2 = \left[\alpha_\theta \sum_m f_m \frac{\partial \xi_z(m)}{\partial Q_i}\right]^2$$

$$= (\alpha_\theta)^2 \sum_n \sum_m f_n f_m \frac{\partial \xi_z(n)}{\partial Q_i} \frac{\partial \xi_z(m)}{\partial Q_i}$$

$$= (\alpha_\theta)^2 \sum_l \langle\langle C_{\mathrm{RR}}(l) C^i_{\xi_z\xi_z}(l)\rangle\rangle (N-l), \tag{31}$$

with

$$\langle\langle C_{\mathrm{RR}}(l) C^i_{\xi_z\xi_z}(l)\rangle\rangle = \frac{1}{N-l} \sum_n^{N-l} f_n f_{n+l} \frac{\partial \xi_z(n)}{\partial Q_i} \frac{\partial \xi_z(n+l)}{\partial Q_i}. \tag{32}$$

Here $\langle\langle \cdots \rangle\rangle$ denotes the average over the site origin n in the chain, and the $N-l$ term arises from the terminal effect of the finite chain. Hence it was found that the bending Raman intensity can be expressed in terms of a convolution of the two correlations $C_{\mathrm{RR}}(n,l) = f_n f_{n+l}$ (called the ring-ring correlation) and $C^i_{\xi_z\xi_z}(n,l) = [\partial\xi_z(n)/\partial Q_i][\partial\xi_z(n+l)/\partial Q_i]$ (the mode-mode correlation).

The approximate formula for the bending Raman spectrum in Eq. (31) strongly suggests that the spectrum will be affected by an occurrence pattern of ringlike atoms along the Se chain due to the presence of the ring-ring correlation factor $C_{\mathrm{RR}}(l)$. To examine this, we carried out a structural analysis on the appearance pattern of ringlike atoms for the 200 disordered-chain samples. Figure 8(a) shows a pattern analysis of seven consecutive atoms along the chain, which include *three* distinct segments or *four* consecutive dihedral angles. [For instance, the RRR configuration in Fig. 8(b) indicates that the three consecutive segments are all ringlike, or equivalently that the four consecutive dihedral angles exhibit the signs $(+, -, +, -)$ or $(-, +, -, +)$.] We see from this figure that the occurrence probability of the RRR configuration is rather small compared to other configurations. One possible explanation for this is that the first and seventh atoms in the RRR configuration tend to overlap with each other, which causes a rather large repulsion energy. To confirm this we evaluated the change in the potential energy of

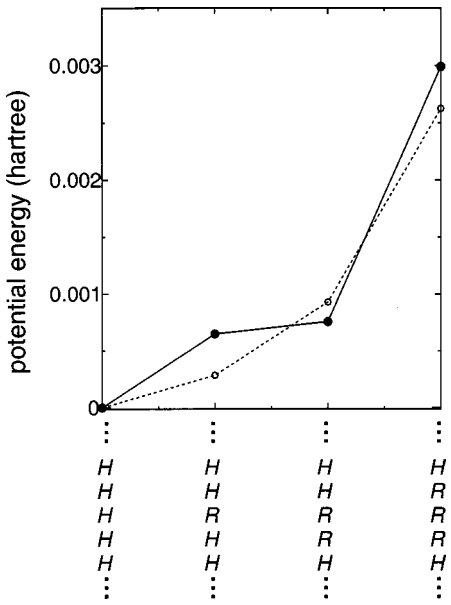

FIG. 9. Change in the total potential energy of the finite chain molecule $HSe_{21}H$ as a function of the number of ringlike atoms (denoted by *R*) contained in the chain. Zero of energy is taken to be the energy of a regular helical chain molecule characterized by all helixlike atoms (*H*). The individual chains are optimized geometrically. Solid and dotted lines are obtained using the *ab initio* RHF method and our model potential, respectively.

the finite Se chain molecule $HSe_{21}H$ as a function of the number of ringlike atoms contained in the chain. Figure 9 displays the potential energy thus obtained using the *ab initio* RHF method (solid line) and our model potential (dotted line), where the geometry of the finite chain was optimized for each configuration. This figure clearly shows a significant increase in energy for the chain with the RRR configuration, thus indicating that this configuration is energetically unstable and tends to be excluded from the sample. Hence we found that *a*-Se has a medium-range order which is related to the steric hindrance effect in the consecutive ringlike segments.

Now we consider how the medium-range order above manifests itself in the bending Raman spectrum. This is investigated by artificially controlling the degree of the medium-range order existing in a model disordered chain and examining the dependence of the Raman spectrum on the former. Specifically, we first introduced a parameter f_{RRR} that characterizes the degree of the steric hindrance effect (or the degree of the medium-range order) in the chain as

$$P_{\mathrm{RRR}}=\frac{1}{8}\times f_{\mathrm{RRR}} \quad (0\leqslant f_{\mathrm{RRR}}\leqslant 1), \tag{33}$$

where P_{RRR} represents the occurrence probability of the RRR configurations. With this definition, $f_{\mathrm{RRR}}=0$ means that there are no RRR configurations while $f_{\mathrm{RRR}}=1$ indicates that it occurs with an equal probability with other configurations listed in Fig. 8(a). Next we created an artificial 216-atom disordered chain by sequentially adding a new atom $n+1$ to the chain consisting of atoms $1\sim n$ according to the following prescription:

(i) The bond length r_n and angle θ_n of the chain were fixed at their equilibrium values, i.e., $r_n=\overline{r}$ and $\theta_n=\overline{\theta}$.

(ii) The magnitude of the dihedral angle $|\phi_n|$ were sampled from the Gaussian distribution with the mean $\overline{\phi}=90°$ and the standard deviation $\delta\phi=40°$. Notice that this distribution corresponds approximately to that of the amorphous samples obtained from the MD simulations in Sec. III.

(iii) The sign of the dihedral angle ϕ_n was determined in a stochastic manner to achieve a given value of f_{RRR}. This was accomplished by setting it to positive or negative with equal probabilities (i.e., $\frac{1}{2}$) except for the case where the preceding dihedral angles exhibit a sign pattern such as $(\phi_{n-3},\phi_{n-2},\phi_{n-1})=(+,-,+)$. In the latter case, the sign of ϕ_n was set to negative with a probability of $f_{\mathrm{RRR}}/2$; i.e., the probability for the four consecutive dihedral angles to become the RRR configuration was artificially reduced as f_{RRR} was decreased.

Then, the reduced polarized Raman spectrum was calculated for the resulting chain using the intrachain valence force field U_{intra} [Eq. (2)] and the BP model [Eq. (16)]. We should note that the nonbonded atoms interaction U_{NB} was not included in the above procedure to avoid a large repulsive energy between overlapping atoms. Figure 7(b) shows the resulting dependence of the bending Raman spectrum on the f_{RRR} parameter above. As seen in the figure the decrease of f_{RRR} shows the effect to make the 80-cm^{-1} peak grow while the 100-cm^{-1} peak become suppressed; i.e., the low-frequency peaks around 80–100 cm^{-1} are strongly correlated with the medium-range order associated with four consecutive dihedral angles. This makes a clear contrast to the case of the static structure factor $S(q)$, for which the details of such medium-range order has little effect on the shape of $S(q)$ as mentioned in Sec. III.

Finally we emphasize that the present results are based entirely on a chain model, i.e., we made an assumption that *a*-Se consists exclusively of two-coordinated polymeric chain. We thus neglected other species such as ring molecules (Se_7 or Se_8) and defects (under- and overcoordinated atoms) in the present analysis. Although as mentioned in the Introduction the fraction of these species is considered to be rather small under the thermodynamic condition studied here, we cannot rule out the possibility that the presence of those species may affect the spectral properties of real *a*-Se. The examination of this effect remains to be explored.

VI. CONCLUSIONS

In this work we have presented a theoretical study on the glassy structure and vibrational spectra of *a*-Se. These properties were investigated in terms of the chain-based model

describing the interaction potential, induced dipole, and induced polarizability of the system. This chain model was constructed on the basis of the *ab initio* MO calculations for various Se clusters. The static structure factor, vibrational density of states, and IR/Raman spectra thus obtained well reproduce the experimental results, despite the simplicity of the model employed in the present work.

The most important result in this paper is that the medium-range order in *a*-Se was revealed (at least partially) through the assignments on the vibrational spectra. The ringlike segments in the disordered chain hardly occur more than three times consecutively as a result of the excluded volume effect, which causes a clear polarized Raman peak at 80 cm^{-1} (this peak is actually observed in the experiment). We think that the present approach which links the structural features of a disordered system to the related spectra is also applicable to other systems, and that it will be helpful in studying a possible medium-range order of those systems.

Finally, we comment on an effect neglected in this work, i.e., a through-space charge transfer between nonbonded atoms. We could not reproduce some peaks in the experimental IR spectrum, which may be attributed to the above neglect of the through-space charge transfer. A straightforward way for incorporating this effect would be to use *ab initio* MD simulations based on density functional theory (DFT). In fact, a variety of disordered systems have already been addressed using such approaches.[55–58] It has also been reported, however, that DFT may provide an inaccurate description of the weak interaction between nonbonded atoms due to the overestimation of the through-space charge transfer.[58] This is particularly the case for *a*-Se or semiconducting liquid Se, in which a large number of artificial defects,[58] which are hardly observed in the experiments, are generated in the simulations. Therefore it is still a highly nontrivial matter whether we can obtain reliable information on *a*-Se (especially that on optical properties such as IR/Raman spectra) using first-principles MD simulations.

ACKNOWLEDGMENTS

The authors are grateful to Takeshi Yamamoto for stimulating discussions and careful reading of the manuscript. We also wish to thank helpful comments by Professor Shigeki Kato. This work was supported by a Grant-in-Aid for Scientific Research from the Ministry of Education.

[1] A. V. Kolobov, H. Oyanagi, Ka. Tanaka, and Ke. Tanaka, Phys. Rev. B **55**, 726 (1997).
[2] A. V. Kolobov, M. Kondo, H. Oyanagi, A. Matsuda, and K. Tanaka, Phys. Rev. B **58**, 12 004 (1998).
[3] H. Hoshino, R. W. Schmutzler, and F. Hensel, Ber. Bunsenges. Phys. Chem. **80**, 27 (1976).
[4] H. Hoshino, R. W. Schmutzler, W. W. Warren, Jr., and F. Hensel, Philos. Mag. **33**, 255 (1976).
[5] J. C. Perron, J. Rabit, and J. F. Rialland, Philos. Mag. **46**, 321 (1982).
[6] W. W. Warren, Jr., and R. Dupree, Phys. Rev. B **22**, 2257 (1980).
[7] K. Tamura and S. Hosokawa, Ber. Bunsenges. Phys. Chem. **96**, 681 (1992).
[8] K. Suzuki and M. Misawa, Inst. Phys. Conf. Ser. **30**, 531 (1977).
[9] R. Bellissent, Nucl. Instrum. Methods Phys. Res. **199**, 289 (1982).
[10] M. Inui, K. Maruyama, S. Takeda, S. Tamaki, and Y. Waseda, J. Phys. Soc. Jpn. **63**, 1378 (1994).
[11] K. Tamura, M. Inui, M. Yao, H. Endo, S. Hosokawa, H. Hoshino, Y. Katayama, and K. Maruyama, J. Phys.: Condens. Matter **3**, 7495 (1991).
[12] J. C. Lasjaunias, A. Ribeyron, and B. Souletie, Solid State Commun. **23**, 745 (1977).
[13] *The Physics of Selenium and Tellurium*, edited by W. C. Cooper (Pergamon, Oxford, 1969).
[14] G. Lucovsky, in *The Physics of Selenium and Tellurium*, edited by E. Gerlach and P. Grosse (Springer-Verlag, New York, 1979), p. 178.
[15] G. Lucovsky and C. W. Wong, Philos. Mag. **52**, 331 (1985).
[16] M. Gorman and S. A. Solin, Solid State Commun. **18**, 1401 (1976).
[17] P. J. Carroll and J. S. Lannin, Solid State Commun. **40**, 81 (1981).
[18] K. Nagata, K. Ishibashi, and Y. Miyamoto, Jpn. J. Appl. Phys. **20**, 463 (1981).
[19] V. N. Bogomolov, V. V. Poborchy, S. G. Romanov, and S. I. Shagin, J. Phys. C **18**, L313 (1985).
[20] C. Bichara, A. Pellegatti, and J. P. Gaspard, Phys. Rev. B **49**, 6581 (1994).
[21] D. Molina, E. Lomba, and G. Kahl, Phys. Rev. B **60**, 6372 (1999).
[22] E. Lomba, D. Molina, and M. Alvarez, Phys. Rev. B **61**, 9314 (2000).
[23] D. Hohl and R. O. Jones, Phys. Rev. B **43**, 3856 (1991).
[24] F. Kirchhoff, G. Kresse, and M. J. Gillan, Phys. Rev. B **57**, 10 482 (1998).
[25] G. Kresse, F. Kirchhoff, and M. J. Gillan, Phys. Rev. B **59**, 3501 (1999).
[26] F. Shimojo, K. Hoshino, M. Watabe, and Y. Zempo, J. Phys.: Condens. Matter **10**, 1199 (1998).
[27] X. Zhang and D. A. Drabold, Phys. Rev. Lett. **83**, 5042 (1999).
[28] R. M. Martin and F. L. Galeener, Phys. Rev. B **23**, 3071 (1981).
[29] K. Nakamura and A. Ikawa, Comput. Phys. Commun. **142**, 295 (2001).
[30] K. Nakamura and A. Ikawa, J. Non-Cryst. Solids **312–314**, 168 (2002).
[31] N. G. Almarza, E. Enciso, and F. J. Bermejo, J. Chem. Phys. **99**, 6876 (1993).
[32] M. García-Hernández, F. J. Bermejo, B. Fåk, J. L. Martínez, E. Enciso, N. G. Almarza, and A. Criado, Phys. Lett. A **175**, 225 (1993).
[33] T. Aoyama, Y. Hiwatari, and A. Ueda, J. Phys. Soc. Jpn. **68**, 857 (1999).
[34] C. Oligschleger and H. R. Schober, Solid State Commun. **93**, 1031 (1995).

[35] C. Oligschleger and J. C. Schön, J. Phys.: Condens. Matter **9**, 1049 (1997).
[36] D. Caprion and H. R. Schober, Phys. Rev. B **62**, 3709 (2000).
[37] M. J. Frisch, G. W. Trucks, H. B. Schlegel, G. E. Scuseria, M. A. Robb, J. R. Cheeseman, V. G. Zakrzewski, J. A. Montgomery, Jr., R. E. Stratmann, J. C. Burant, S. Dapprich, J. M. Millam, A. D. Daniels, K. N. Kudin, M. C. Strain, O. Farkas, J. Tomasi, V. Barone, M. Cossi, R. Cammi, B. Mennucci, C. Pomelli, C. Adamo, S. Clifford, J. Ochterski, G. A. Peterson, P. Y. Ayala, Q. Cui, K. Morokuma, A. D. Malick, K. D. Rabuck, K. Raghavachari, J. B. Foresman, J. Cioslowski, J. V. Ortiz, B. B. Stefanov, G. Liu, A. Liashenko, P. Piskorz, I. Komaroni, R. Gomperts, R. L. Martin, D. J. Fox, T. Keith, M. A. Al-Laham, C. Y. Peng, A. Nanayakkara, M. Challacombe, P. M. W. Gill, B. Johnson, W. Chen, M. W. Wong, J. L. Andres, C. Gonzalez, M. HeadGordon, E. S. Replogle, and J. A. Pople, GAUSSIAN 98, Revision A.6 (Gaussian, Inc., Pittsburgh, 1998).
[38] W. J. Stevens, M. Krauss, H. Basch, and P. G. Jasien, Can. J. Chem. **70**, 612 (1992).
[39] *Gaussian Basis Sets for Molecular Calculations*, edited by S. Hujinaga (Elsevier, Amsterdam, 1984).
[40] K. Nakamura and A. Ikawa, Phys. Rev. B **66**, 024420 (2002).
[41] R. M. Martin, G. Lucovsky, and K. Helliwell, Phys. Rev. B **13**, 1383 (1976).
[42] *Handbook of Chemistry and Physics*, 82nd ed., edited by D. R. Lide (CRC, Boca Raton).
[43] W. C. Swope, H. C. Andersen, P. Berens, and K. R. Wilson, J. Chem. Phys. **76**, 637 (1982).
[44] R. Fletcher and C. M. Reevs, Comput. J. (UK) **7**, 149 (1964).
[45] W. A. Kamitakahara, taken from X. Zhang and D. A. Drabold, Phys. Rev. Lett. **83**, 5042 (1999).
[46] R. Alben, D. Weaire, J. E. Smith, Jr., and M. H. Brodsky, Phys. Rev. B **11**, 2271 (1975).
[47] K. Winer and M. Cardona, Phys. Rev. B **35**, 8189 (1987).
[48] K. Machida, *Principles of Molecular Mechanics* (Wiley, New York, 1999).
[49] C. E. Check, T. O. Faust, J. M. Bailey, B. J. Wright, T. M. Gilbert, and L. S. Sunderlin, J. Phys. Chem. A **105**, 8111 (2001).
[50] M. D. Halls and H. B. Schlegel, J. Chem. Phys. **111**, 8819 (1999).
[51] M. A. Eliashevich and M. V. Wolkenstein, J. Phys. (Moscow) **9**, 101 (1944).
[52] P. W. Higgs, Proc. R. Soc. London, Ser. A **220**, 472 (1953).
[53] The rotational angle τ of the regular helix can be expressed using the equilibrium bond angle $\overline{\theta}$ and dihedral angle $\overline{\phi}$ as $\tau = \cos^{-1}[\frac{1}{2}(-\cos\overline{\theta}+\cos\overline{\phi}-\cos\overline{\theta}\cos\overline{\phi}-1)]$, and thus gives $\tau = 111.2°$ with $\overline{\theta}=106.0°$ and $\overline{\phi}=90.0°$ (Table II).
[54] We note that the coupling $k_{rr'}$ and $k_{r\theta}$ terms and the equilibrium bond angle $\overline{\theta}$ play important roles in obtaining the convex shape of the stretching phonon dispersion.
[55] A. Pasquarello and R. Car, Phys. Rev. Lett. **79**, 1766 (1997).
[56] P. L. Silvestrelli, M. Bernasconi, and M. Parrinello, Chem. Phys. Lett. **277**, 478 (1997).
[57] A. Debernardi, M. Bernasconi, M. Cardona, and M. Parrinello, Appl. Phys. Lett. **71**, 2692 (1997).
[58] G. Kresse, J. Non-Cryst. Solids **312-314**, 52 (2002).